Low Gilbert damping in epitaxial thin films of the nodal-line semimetal D0₃-Fe₃Ga

Shoya Sakamoto ,^{1,*} Tomoya Higo ,^{1,2} Shingo Tamaru ,³ Hitoshi Kubota ,³ Kay Yakushiji ,^{2,3} Satoru Nakatsuji ,^{1,2,4,5} and Shinji Miwa ,^{1,2,5,†}

¹The Institute for Solid State Physics, The University of Tokyo, Kashiwa, Chiba 277-8581, Japan

²CREST, Japan Science and Technology Agency (JST), 4-1-8 Honcho Kawaguchi, Saitama 332-0012, Japan

³National Institute of Advanced Industrial Science and Technology (AIST), Research Center for Emerging Computing Technologies,

Tsukuba, Ibaraki 305-8568, Japan

⁴Department of Physics, University of Tokyo, Hongo, Bunkyo, Tokyo 113-0033, Japan ⁵Trans-scale Quantum Science Institute, The University of Tokyo, Bunkyo, Tokyo 113-0033, Japan



(Received 12 January 2021; accepted 30 March 2021; published 20 April 2021)

 $D0_3$ -ordered Fe₃Ga has been recently reported to show a giant anomalous Nernst effect due to a large Berry curvature along the interconnected nodal lines concentrated near the Fermi level. This peculiar band structure may be advantageous for spintronics device applications because one can expect a strong response to a gate-voltage application. This study evaluates the Gilbert damping constants, a key parameter governing the magnetization dynamics of epitaxial thin films of $D0_3$ -Fe₃Ga and bcc-Fe by ferromagnetic resonance measurements. We find that the Gilbert damping constant of $D0_3$ -Fe₃Ga $[(6.0 \pm 0.2) \times 10^{-3}]$ is relatively low and comparable to that of Fe $[(2.3 \pm 0.2) \times 10^{-3}]$. The low Gilbert damping suggests that the interconnected nodal lines near the Fermi level do not hinder magnetization dynamics, making $D0_3$ -Fe₃Ga even more attractive as a building block of spintronics devices.

DOI: 10.1103/PhysRevB.103.165122

I. INTRODUCTION

In recent years, there has been growing interest in physical phenomena associated with the nonvanishing Berry curvature of Bloch states [1]. The anomalous Hall effect (AHE) and anomalous Nernst effect (ANE) are typical examples: AHE results from the summation of the Berry curvature of all occupied states [1,2], and ANE results from the Berry curvature of bands near the Fermi level [1,3]. Indeed, exceptionally large AHE and ANE were observed in ferromagnetic Weyl semimetals such as Co₂MnGa [4,5] and Co₃Sn₂S₂ [6,7] and also in antiferromagnetic Weyl semimetals such as Mn₃Sn [8,9] and Mn₃Ge [10,11], where there is claimed to be a large Berry curvature around the Weyl nodes.

Although not a Weyl semimetal, $D0_3$ -ordered Fe₃Ga has been recently reported to show a giant ANE of 6 μ V/K [12], close to the highest values reported thus far and 20 times stronger than that of α -Fe. $D0_3$ -Fe₃Ga consists of only two elements and has a simple cubic structure, as shown in Fig. 1(a), and therefore, it is relatively easy to fabricate even in a thin-film form. These features make $D0_3$ -Fe₃Ga promising for the realization of low-cost and flexible thermoelectric generators. The origin of the giant ANE was attributed to the large density of states (DOS) and Berry curvature along the quasi-two-dimensional (2D) network of gapped nodal lines (referred to as nodal web). The nodal web consists of two nearly flat valence and conduction bands touching each other

that acquire a large Berry curvature when the spin-orbit interaction gaps the intersections. The large density of states and Berry curvature at the Fermi level may be useful for spintronics device applications because a gate voltage may effectively modulate the Berry-curvature-associated response as well as magnetic anisotropy. In this respect, characterizing the magnetic damping, which governs magnetization dynamics, is of great importance [13,14]. It is worth mentioning that Fe-Ga alloys (galfenol) also show a sizable ANE [15] and are famous for their large magnetostriction [16–19]. These aspects may also be advantageous for applications.

In the present study, we perform ferromagnetic resonance (FMR) measurements on epitaxial thin films of $D0_3$ -Fe₃Ga and bcc Fe to characterize their magnetic damping. The intrinsic Gilbert damping constant of Fe₃Ga is deduced to be $(6.0 \pm 0.2) \times 10^{-3}$, which is relatively low and comparable to the Fe value of $(2.3 \pm 0.2) \times 10^{-3}$. The low Gilbert damping constant makes $D0_3$ -Fe₃Ga even more attractive for device applications that involve magnetization switching.

II. EXPERIMENT AND CALCULATION

Fe and Fe $_3$ Ga thin films were grown on MgO(001) substrates by molecular beam epitaxy (MBE) and dc magnetron sputtering, respectively. The sample structures are schematically shown in Fig. 1(b). The substrates were annealed at 800 °C for 10 min before the deposition. For the Fe thin film, a 5-nm-thick MgO seed layer was first grown at a rate of 0.1 Å/s, and a 50-nm-thick Fe layer was grown at a rate of 0.2 Å/s. The sample was annealed at 350 °C for 30 min and covered by a 5-nm-thick MgO layer deposited at a rate

^{*}Corresponding author: shoya.sakamoto@issp.u-tokyo.ac.jp

[†]Corresponding author: miwa@issp.u-tokyo.ac.jp

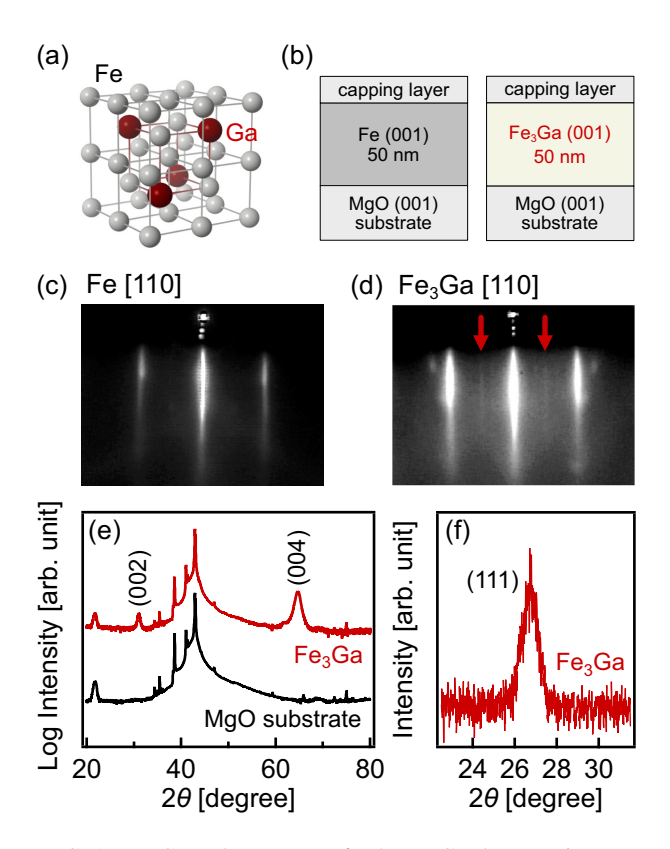


FIG. 1. (a) Crystal structure of $D0_3$ -Fe₃Ga drawn using VESTA [20]. (b) Thin-film structures. (c) and (d) In situ reflection highenergy electron diffraction images of the annealed Fe and Fe₃Ga surfaces taken along the Fe [110] and Fe₃Ga [110] (or MgO [100]) direction. (e) Out-of-plane $2\theta/\omega$ x-ray diffraction (XRD) patterns of the Fe₃Ga thin film and an MgO (001) substrate. (f) Fe₃Ga (111) superlattice peak is detected by an $2\theta/\omega$ scan, indicating the $D0_3$ ordering of Fe₃Ga.

of 0.1 Å/s. For the Fe₃Ga thin film, a 50-nm-thick Fe₃Ga layer was directly grown on an MgO substrate at a rate of 0.4 Å/s and annealed at 500 °C for 30 min. The 2-nm-thick MgO and 5-nm-thick AlO_x capping layers were grown at a rate of 0.1 Å/s. This Fe₃Ga growth procedure is the same as in our previous report [12]: We used the same apparatuses, the same growth rate, and the same annealing temperature and time. Note that only the Fe₃Ga layer was grown by sputtering and the other layers were grown by MBE. Both sputtering and MBE chambers are connected, and all the deposition was conducted without exposing the samples to air. The base pressures of the sputtering and MBE chambers were below 5×10^{-7} and 3×10^{-8} Pa, respectively.

We conducted FMR measurements using a vector network analyzer and a coplanar waveguide (CPW). The width and the thickness of the center conductor were 200 and 12 μ m, respectively, and the gap between the center conductor and the ground was 60 μ m. The 20- μ m-thick polyester tape was inserted between the CPW and the samples. Unlike a conventional measurement setup, the magnetic field was modulated by ± 0.48 mT at each magnetic field H, and the magnetic-field derivative of the transmission coefficient S_{21} , namely $\Delta S_{21} = S_{21}(H+0.48 \text{ mT}) - S_{21}(H-0.48 \text{ mT})$, was measured. This field-modulation technique gives background-free FMR

spectra and enables precise estimation of FMR peak positions and peak widths even when the signals are weak [21]. Note that it is confirmed that the field-modulation technique yields essentially the same FMR peak positions and widths as the conventional field-sweep technique. All the FMR measurements were performed at room temperature. Magnetic fields up to \sim 2 T were applied to the [100], [110], and [001] directions of Fe₃Ga and Fe.

To discuss the relationship between the DOS and the Gilbert damping constants of Fe and $D0_3$ -Fe₃Ga, we performed density-functional-theory (DFT) calculations under the Perdew-Burke-Ernzerhof generalized gradient approximation using the WIEN2K package [22]. The experimental lattice constants of 2.87 and 5.80 Å [12] were used for Fe and $D0_3$ -Fe₃Ga, respectively. A spin-orbit interaction was included. Brillouin-zone integration was performed on a $17 \times 17 \times 17$ k-point mesh.

III. RESULTS

Figures 1(c) and 1(d) show the in situ reflection highenergy electron diffraction (RHEED) images of the annealed Fe and Fe₃Ga surfaces. The sharp streak patterns guarantee the epitaxial growth of Fe and Fe₃Ga layers. In addition to the main intense streaks, the RHEED image of Fe₃Ga shows weak streaks in between marked by the red arrows in Fig. 1(d). We attribute the weak streaks to the superlattice diffraction from the $\sqrt{2} \times \sqrt{2}$ Ga arrangement on the $D0_3$ -Fe₃Ga surface. The crystallinity of the Fe₃Ga thin film is also evaluated by performing x-ray diffraction (XRD) measurements. The out-of-plane XRD $2\theta/\omega$ pattern [Fig. 1(e)] does not show any unknown second-phase peaks but only shows the Fe₃Ga (002) and (004) peaks. This second-phase-free XRD pattern together with the streaky RHEED image indicate the singlecrystalline epitaxial growth of the Fe₃Ga layer. Note that an XRD ϕ scan (not shown) exhibits a fourfold symmetric pattern accordingly. The $D0_3$ ordering is confirmed by the $2\theta/\omega$ XRD pattern [Fig. 1(f)] that exhibits the $D0_3$ -specific (111) peak. From the XRD (111) and (004) [or (002)] peaks, the in-plane and out-of-plane lattice constants are estimated to be 5.788 and 5.761 Å, respectively. The longer in-plane lattice constant is consistent with the fact that there is tensile epitaxial strain from the MgO substrate caused by \sim 3% lattice mismatch.

Figures 2(a) and 2(b) show typical FMR spectra of the Fe and Fe₃Ga thin films, respectively. Here, an FMR spectrum refers to ΔS_{21} as a function of magnetic field (H) at a fixed frequency. In order to deduce the FMR peak position (H_r) and peak width (ΔH), we fit the following function to each spectrum [23,24],

$$\Delta S_{21} = S(H + 0.48 \text{ mT}) - S(H - 0.48 \text{ mT}),$$
 (1)

$$S(H) = \frac{A}{H_{\rm r}^2 - H(H - i\Delta H)} e^{i\phi}.$$
 (2)

Here, A represents the amplitude of the signals, and $e^{i\phi}$ accounts for a phase shift. Equation (2) can be approximated as the summation of the Lorentzian and antisymmetric Lorentzian functions when $\Delta H \ll H_{\rm r}$, and ΔH corresponds to the full width at half maximum of the Lorentzian

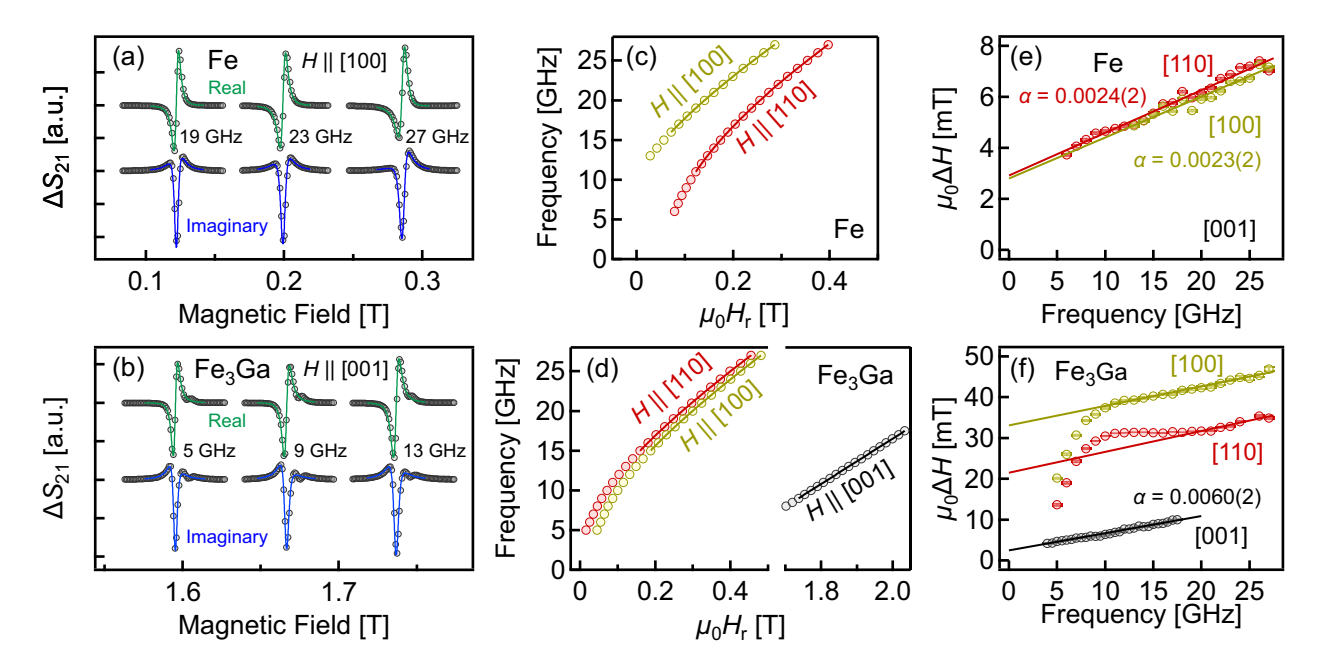


FIG. 2. (a) and (b) Typical ferromagnetic resonance (FMR) spectra of the Fe and Fe₃Ga thin films. The solid curves are the fit of Eqs. (1) and (2). (c) and (d) Resonance frequency plotted against resonance magnetic fields. The solid curves are the fit of Eqs. (4)–(6). (e) and (f) FMR peak width as a function of the resonance frequency. The data are fitted by a linear function (solid lines), the slope of which represents the intrinsic Gilbert damping constant.

component. The fitted curves reproduce the experimental spectra very well, as shown in Figs. 2(a) and 2(b) by solid curves.

Figures 2(c) and 2(d) show the deduced FMR peak positions for the Fe and Fe₃Ga thin films as a function of microwave frequency. We did not perform out-of-plane FMR measurements for the Fe thin film because the saturation magnetization was too large for the present experimental setup.

In thin-film samples, the crystal symmetry is lowered from cubic to tetragonal because of the epitaxial strain from the substrate. Under the tetragonal symmetry, the total energy of the system can be written as [25]

$$E = \mu_0 M_s H [\cos \theta \cos \theta_H + \sin \theta \sin \theta_H \cos(\phi - \phi_H)]$$

$$- \frac{1}{2} \mu_0 M_s^2 \sin^2 \theta - K_{2\perp} \cos^2 \theta$$

$$- \frac{1}{2} K_{4\perp} \cos^4 \theta - \frac{1}{2} K_{4\parallel} \frac{1}{4} (3 + \cos 4\phi) \sin^4 \theta,$$
 (3)

where μ_0 is the vacuum permeability, and M_s is the saturation magnetization. θ (θ_H) denotes the tilt angle between the [001] direction and the magnetization (magnetic-field) direction, and ϕ (ϕ_H) denotes the azimuth angle of the magnetization (magnetic field) with respect to the [100] direction. $K_{2\perp}$, $K_{4\perp}$, and $K_{4\parallel}$ represent the out-of-plane uniaxial, out-of-plane cubic, and in-plane cubic magnetocrystalline anisotropy energy, respectively. Based on Eq. (3), the relationship between the resonance magnetic field and frequency can be written as [25,26]

$$f_{\rm r}^{[100]} = \frac{\mu_0 \gamma}{2\pi} \sqrt{(H_{\rm r} + H_{4\parallel})(H_{\rm r} + M_{\rm eff} + H_{4\parallel})},$$
 (4)

$$f_{\rm r}^{[110]} = \frac{\mu_0 \gamma}{2\pi} \sqrt{(H_{\rm r} - H_{4\parallel})(H_{\rm r} + M_{\rm eff} + H_{4\parallel}/2)}, \quad (5)$$

$$f_{\rm r}^{[001]} = \frac{\mu_0 \gamma}{2\pi} (H_{\rm r} - M_{\rm eff} + H_{4\perp}).$$
 (6)

Here, $f_{\rm r}$ denotes the resonance frequency with its superscript representing the magnetic-field direction. γ is the gyromagnetic ratio expressed as $\gamma = g\mu_{\rm B}/\hbar$, where g is the Landé g-factor, $\mu_{\rm B}$ is the Bohr magneton, and \hbar is the reduced Planck constant. $M_{\rm eff}$ is the effective saturation magnetization defined as $M_{\rm eff} = M_{\rm S} - H_{2\perp}$. $H_{2\perp}$, $H_{4\parallel}$, and $H_{4\perp}$ are the anisotropy fields defined as $H_i = 2K_i/\mu_0 M_{\rm S}$.

Table I summarizes g-factors, $M_{\rm eff}$, and $H_{4\parallel}$ deduced by fitting Eqs. (4)–(6) to the data. Here, $M_{\rm eff}$ for the Fe₃Ga [001] direction is obtained assuming $H_{4\perp}=H_{4\parallel}\sim-15.5$ mT. Note that $M_{\rm eff}\simeq M_{\rm s}$ (or $H_{2\perp}\ll M_{\rm s}$) because almost the same inplane and out-of-plane lattice constants would not induce significant uniaxial magnetic anisotropy. In fact, the obtained $M_{\rm eff}$ of \sim 1.43 T is in good agreement with the saturation magnetization of bulk $D0_3$ -Fe₃Ga at 300 K, 1.42 T [12]. We find that the g-factors of Fe and Fe₃Ga are almost the same within error bars. On the other hand, the in-plane cubic

TABLE I. The results of the fitting using Eqs. (4)–(7): *g*-factors (*g*), in-plane cubic anisotropy fields ($H_{4||}$), effective saturation magnetizations ($M_{\rm eff}$), intrinsic Gilbert damping constants (α), and the inhomogeneous line broadening (ΔH_0). The numbers in parentheses refer to the fitting errors.

	Fe		Fe ₃ Ga		
	[100]	[110]	[100]	[110]	[001]
g	2.07(4)	2.05(3)	2.08(3)	2.08(4)	2.05(1)
$\mu_0 H_{4 }$ (mT)	62(2)	60(1)	-20(3)	-11(4)	
$\mu_0 M_{\rm eff}$ (T)	2.15(9)	2.18(8)	1.46(6)	1.40(8)	1.43(2)
$\alpha \times 10^{-3}$	2.3(2)	2.4(2)	6.9(4)	7.4(9)	6.0(2)
$\frac{\mu_0 \Delta H_0 \text{ (mT)}}{}$	2.8(2)	2.9(2)	33(1)	22(3)	2.5(1)

magnetic anisotropy $K_{4\parallel}$ of Fe₃Ga is about seven times weaker than that of Fe, and the sign is opposite. The [110] easy axis seems intrinsic to the $D0_3$ -ordered Fe₃Ga because the previous FMR study reported that disordered Fe₈₁Ga₁₉ thin films have a sizable positive (or [100] easy axis) $H_{4\parallel}$ of 75–100 mT [27]. This difference in magnetic anisotropy indicates that the $D0_3$ atomic ordering significantly alters the electronic band structure of Fe-Ga alloys and induces the giant ANE as a result [12].

Figures 2(e) and 2(f) show the deduced FMR peak widths plotted against the resonance frequency. Here, the slope of the data represents the intrinsic Gilbert damping constant α , while the y intercept (ΔH_0) represents extrinsic linewidth broadening caused by inhomogeneous (resonance) magnetic-field distribution. That is,

$$\mu_0 \Delta H = \mu_0 \Delta H_0 + \frac{4\pi\alpha}{\gamma} f_r. \tag{7}$$

The linear fitting with Eq. (7) yields the Fe Gilbert damping constant of $\alpha = 0.0023$, which is as low as the previously reported $\alpha \sim 0.0023$ [28,29]. This agreement implies that the radiative damping [30] is not significant in the present study.

The linear relationship does not hold for the Fe₃Ga data taken with in-plane magnetic fields: The data show a steep increase (with a hump) at low frequencies. We attribute this nonlinear behavior to the two-magnon scattering (TMS) [31–33], where a uniform-precession magnon with k = 0 scatters into another energetically degenerate magnon with $k \neq 0$. The TMS occurs when some inhomogeneity, which would be related to the surface roughness or the grain structure in the present case, breaks translational symmetry and makes the crystal momentum (k) nonconserved.

The measurements with out-of-plane magnetic fields do not suffer from the TMS as there is no $k \neq 0$ magnon to scatter into [34]. The intrinsic Gilbert damping of the $D0_3$ -Fe₃Ga thin film is thus estimated to be 0.0060(2). The intrinsic Gilbert damping constants (α) and extrinsic linewidth broadening (ΔH_0) of Fe and $D0_3$ -Fe₃Ga are listed in Table I. The extrinsic linewidth broadening for the Fe₃Ga [001] direction is deduced to be 2.5 mT, which is as small as the Fe values. This small extrinsic broadening suggests that there is no significant inhomogeneity in the resonance magnetic field distribution.

The Gilbert damping constant, or the relaxation frequency $G = \alpha \gamma M_s$, can be roughly approximated as $G \sim$ $\xi^2 D(E_{\rm F})$ [32], where ξ and $D(E_{\rm F})$ represent the spin-orbit coupling strength and the DOS at the Fermi level, respectively. Figures 3(a) and 3(b) show the calculated spin-resolved DOS of Fe and D0₃-Fe₃Ga, respectively. The DOS of D0₃-Fe₃Ga is markedly different from that of Fe and show sharp flatband features. Figure 3(c) shows the total DOS of Fe and D03-Fe3Ga per unit-cell volume of bcc Fe. The total DOS of D03-Fe3Ga at the Fermi level relative to that of Fe $[D_{\text{Fe}_3\text{Ga}}(E_{\text{F}})/D_{\text{Fe}}(E_{\text{F}})]$ falls within the range of 0.7–1.7 with a Fermi-level shift of ± 130 meV. Assuming the same ξ for both Fe₃Ga and Fe, the ratio $G_{\text{Fe}_3\text{Ga}}/G_{\text{Fe}}$ also becomes 0.7-1.7, which is in fair agreement with the experimental value of 1.7. This agreement suggests that the Ga inclusion does not significantly increase the spin-orbit coupling strength probably because Ga is nonmagnetic and does not have states near the Fermi level. To be more precise, the ratio $\xi_{\text{Fe}_3\text{Ga}}/\xi_{\text{Fe}}$ should be

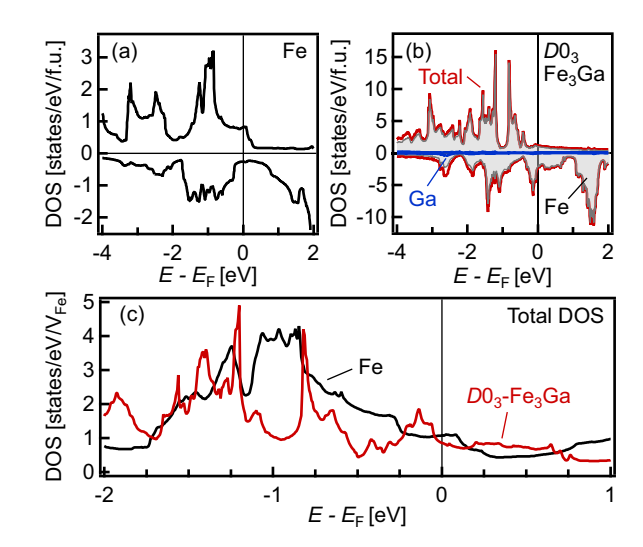


FIG. 3. (a) and (b) Spin-resolved densities of states (DOS) of Fe and $D0_3$ -Fe₃Ga per formula unit. The positive and negative signs represent the majority-spin and minority-spin states, respectively. (c) Total DOS of Fe and $D0_3$ -Fe₃Ga per unit-cell volume of bcc Fe ($V_{\rm Fe}$).

in the range of 1–1.6. Note that the magnetostrictive responses of Fe₃Ga may partially contribute to the enhanced damping.

Although the intrinsic Gilbert damping constant of $D0_3$ -Fe₃Ga is larger than that of Fe, it is still low compared to those of typical ferromagnets: 0.0005–0.003 for FeCo alloys [28], 0.004–0.006 for CoFeB [35–37], ~0.007 for Permalloy [38,39], and 0.0065 for disordered A2-Fe₈₁Ga₁₉ [27]. In other words, the nodal web with a large Berry curvature near the Fermi level does not hinder the magnetization dynamics much. The low Gilbert damping may be useful for spintronics device applications because one may be able to efficiently switch magnetization by exploiting the peculiar band structure of $D0_3$ -Fe₃Ga. For an application, it is important to realize low absolute damping. Thus, while the TMS would be less of an issue when devices are made smaller than the magnon wavelength, the sample growth process might have to be further optimized to suppress the TMS.

IV. CONCLUSION

We have investigated the magnetization dynamics of the epitaxial thin films of the nodal-line semimetal $D0_3$ -Fe₃Ga by ferromagnetic resonance measurements. We have deduced the intrinsic Gilbert damping constant of $D0_3$ -Fe₃Ga to be $(6.0 \pm 0.2) \times 10^{-3}$, which is larger than the Fe Gilbert damping constant of $(2.3 \pm 0.2) \times 10^{-3}$ but as low as other typical ferromagnets. The low Gilbert damping and the peculiar band structure with a large Berry curvature make $D0_3$ -Fe₃Ga attractive as a building block of spintronics devices.

ACKNOWLEDGMENTS

This work was supported by JSPS KAKENHI (No. JP18H03880, No. JP19H00650, No. JP20K15158), JST CREST (JPMJCR18T3), JST-Mirai Program (JPMJMI20A1), the Murata Science Foundation, and the Spintronics Research Network of Japan (Spin-RNJ).

- [1] D. Xiao, M.-C. Chang, and Q. Niu, Rev. Mod. Phys. 82, 1959 (2010)
- [2] N. Nagaosa, J. Sinova, S. Onoda, A. H. MacDonald, and N. P. Ong, Rev. Mod. Phys. 82, 1539 (2010).
- [3] D. Xiao, Y. Yao, Z. Fang, and Q. Niu, Phys. Rev. Lett. 97, 026603 (2006).
- [4] A. Sakai, Y. P. Mizuta, A. A. Nugroho, R. Sihombing, T. Koretsune, M.-T. Suzuki, N. Takemori, R. Ishii, D. Nishio-Hamane, R. Arita *et al.*, Nat. Phys. 14, 1119 (2018).
- [5] S. N. Guin, K. Manna, J. Noky, S. J. Watzman, C. Fu, N. Kumar, W. Schnelle, C. Shekhar, Y. Sun, J. Gooth, and C. Felser, NPG Asia Mater. 11, 16 (2019).
- [6] E. Liu, Y. Sun, N. Kumar, L. Muechler, A. Sun, L. Jiao, S.-Y. Yang, D. Liu, A. Liang, Q. Xu, J. Kroder, V. Süß, H. Borrmann, C. Shekhar, Z. Wang, C. Xi, W. Wang, W. Schnelle, S. Wirth, Y. Chen *et al.*, Nat. Phys. 14, 1125 (2018).
- [7] Q. Wang, Y. Xu, R. Lou, Z. Liu, M. Li, Y. Huang, D. Shen, H. Weng, S. Wang, and H. Lei, Nat. Commun. 9, 3681 (2018).
- [8] S. Nakatsuji, N. Kiyohara, and T. Higo, Nature (London) 527, 212 (2015).
- [9] M. Ikhlas, T. Tomita, T. Koretsune, M.-T. Suzuki, D. Nishio-Hamane, R. Arita, Y. Otani, and S. Nakatsuji, Nat. Phys. 13, 1085 (2017).
- [10] N. Kiyohara, T. Tomita, and S. Nakatsuji, Phys. Rev. Appl. 5, 064009 (2016).
- [11] A. Nayak, J. Fischer, Y. Sun, B. Yan, J. Karel, A. Komarek, C. Shekhar, N. Kumar, W. Schnelle, J. Kübler, C. Felser, and S. Parkin, Sci. Adv. 2, e1501870 (2016).
- [12] A. Sakai, S. Minami, T. Koretsune, T. Chen, T. Higo, Y. Wang, T. Nomoto, M. Hirayama, S. Miwa, D. Nishio-Hamane, F. Ishii, R. Arita, and S. Nakatsuji, Nature (London) 581, 53 (2020).
- [13] D. Ralph and M. Stiles, J. Magn. Magn. Mater. 320, 1190 (2008).
- [14] S. Bhatti, R. Sbiaa, A. Hirohata, H. Ohno, S. Fukami, and S. Piramanayagam, Mater. Today 20, 530 (2017).
- [15] H. Nakayama, K. Masuda, J. Wang, A. Miura, K.-i. Uchida, M. Murata, and Y. Sakuraba, Phys. Rev. Materials 3, 114412 (2019).
- [16] A. E. Clark, J. B. Restorff, M. Wun-Fogle, T. A. Lograsso, and D. L. Schlagel, IEEE Trans. Magn. 36, 3238 (2000).
- [17] R. Wu, J. Appl. Phys. 91, 7358 (2002).
- [18] J. Atulasimha and A. B. Flatau, Smart Mater. Struct. 20, 043001 (2011).
- [19] M. V. Matyunina, M. A. Zagrebin, V. V. Sokolovskiy, O. O. Pavlukhina, V. D. Buchelnikov, A. M. Balagurov, and I. S. Golovin, Phase Transitions 92, 101 (2018).
- [20] K. Momma and F. Izumi, J. Appl. Crystallogr. 44, 1272 (2011).

- [21] S. Tamaru, S. Tsunegi, H. Kubota, and S. Yuasa, Rev. Sci. Instrum. 89, 053901 (2018).
- [22] P. Blaha, K. Schwarz, G. Madsen, D. Kvasnicka, and J. Luitz, WIEN2k: An Augmented Plane Wave+ Local Orbitals Program for Calculating Crystal Properties (Technical Universität, Wien Austria, 2001).
- [23] S. S. Kalarickal, P. Krivosik, M. Wu, C. E. Patton, M. L. Schneider, P. Kabos, T. J. Silva, and J. P. Nibarger, J. Appl. Phys. 99, 093909 (2006).
- [24] A. Conca, S. Keller, L. Mihalceanu, T. Kehagias, G. P. Dimitrakopulos, B. Hillebrands, and E. T. Papaioannou, Phys. Rev. B 93, 134405 (2016).
- [25] M. Farle, Rep. Prog. Phys. 61, 755 (1998).
- [26] X. Liu, Y. Sasaki, and J. K. Furdyna, Phys. Rev. B 67, 205204 (2003).
- [27] S. Budhathoki, A. Sapkota, K. M. Law, B. Nepal, S. Ranjit, S. KC, T. Mewes, and A. J. Hauser, J. Magn. Magn. Mater. 496, 165906 (2020).
- [28] M. A. W. Schoen, D. Thonig, M. L. Schneider, T. J. Silva, H. T. Nembach, O. Eriksson, O. Karis, and J. M. Shaw, Nat. Phys. 12, 839 (2016).
- [29] B. Khodadadi, A. Rai, A. Sapkota, A. Srivastava, B. Nepal, Y. Lim, D. A. Smith, C. Mewes, S. Budhathoki, A. J. Hauser, M. Gao, J.-F. Li, D. D. Viehland, Z. Jiang, J. J. Heremans, P. V. Balachandran, T. Mewes, and S. Emori, Phys. Rev. Lett. 124, 157201 (2020).
- [30] M. A. W. Schoen, J. M. Shaw, H. T. Nembach, M. Weiler, and T. J. Silva, Phys. Rev. B 92, 184417 (2015).
- [31] R. Arias and D. L. Mills, Phys. Rev. B 60, 7395 (1999).
- [32] S. Mizukami, D. Watanabe, M. Oogane, Y. Ando, Y. Miura, M. Shirai, and T. Miyazaki, J. Appl. Phys. 105, 07D306 (2009).
- [33] W. K. Peria, T. A. Peterson, A. P. McFadden, T. Qu, C. Liu, C. J. Palmstrøm, and P. A. Crowell, Phys. Rev. B 101, 134430 (2020).
- [34] P. Landeros, R. E. Arias, and D. L. Mills, Phys. Rev. B 77, 214405 (2008).
- [35] C. Bilzer, T. Devolder, J.-V. Kim, G. Counil, C. Chappert, S. Cardoso, and P. P. Freitas, J. Appl. Phys. 100, 053903 (2006).
- [36] X. Liu, W. Zhang, M. J. Carter, and G. Xiao, J. Appl. Phys. 110, 033910 (2011).
- [37] A. Conca, J. Greser, T. Sebastian, S. Klingler, B. Obry, B. Leven, and B. Hillebrands, J. Appl. Phys. 113, 213909 (2013).
- [38] C. Luo, Z. Feng, Y. Fu, W. Zhang, P. K. J. Wong, Z. X. Kou, Y. Zhai, H. F. Ding, M. Farle, J. Du, and H. R. Zhai, Phys. Rev. B 89, 184412 (2014).
- [39] Y. Zhao, Q. Song, S.-H. Yang, T. Su, W. Yuan, S. S. P. Parkin, J. Shi, and W. Han, Sci. Rep. 6, 22890 (2016).